

[LiCl₂]⁻ Superhalide: A New Charge Carrier for Graphite Cathode of Dual-Ion Batteries

*Keun-il Kim^[a], Longteng Tang^[a], Pegah Mirabedini^[b], Amika Yokoi^[c], Jesse M. Muratli^[d],
Qiubo Guo^[a], Prof. Michael M. Lerner^[a], Prof. Kazuma Gotoh^[c]*, Prof. P. Alex Greaney^[b]*,
Prof. Chong Fang^[a]* and Prof. Xiulei Ji^[a]**

[a] Department of Chemistry
Oregon State University
Corvallis, Oregon 97331-4003, United States
E-mail: david.ji@oregonstate.edu
chong.fang@oregonstate.edu

[b] Department of Materials Science and Engineering
University of California, Riverside
California 92521, United States
E-mail: agreaney@engr.ucr.edu

[c] Graduate School of Natural Science & Technology
Okayama University
3-1-1 Tsushima-Naka, Okayama 700-8530, Japan
E-mail: kgotoh@okayama-u.ac.jp

Keywords: anion insertion, DES electrolytes, dual-ion batteries, graphite oxidation, superhalides

Abstract

New acceptor type graphite intercalation compounds (GICs) offer candidates of cathode materials for dual-ion batteries, where superhalides represent the emerging anion charge carriers for such batteries. Here, we report the reversible insertion of [LiCl₂]⁻ into graphite from an aqueous deep eutectic solvent electrolyte of 20 *m* LiCl + 20 *m* choline chloride. [LiCl₂]⁻ is the primary anion species in this electrolyte as revealed by the femtosecond stimulated Raman spectroscopy results, particularly through the rarely observed H–O–H bending mode. The insertion of Li-Cl anionic species is suggested by ⁷Li Magic Angle Spinning nuclear magnetic resonance results that describe a unique chemical environment of Li⁺ ions with electron donors around. ²H nuclear magnetic resonance results further suggest that water molecules are co-

inserted into graphite. Density functional theory calculations reveal that the anionic insertion of hydrated $[\text{LiCl}_2]^-$ takes place at a lower potential, being more favorable. X-ray diffraction and the Raman results show that the insertion of $[\text{LiCl}_2]^-$ creates turbostratic structure in graphite instead of forming long-range ordered GICs. The storage of $[\text{LiCl}_2]^-$ in graphite as a cathode for dual-ion batteries offers a capacity of 114 mAh g^{-1} that is stable over 440 cycles.

1. Introduction

Dual-ion batteries (DIBs) differ from rocking-chair batteries by operating like a playing accordion, where during charging anions and cations from the electrolyte get inserted into cathode and anode, respectively, and during discharging these ions are released back to the electrolyte.^[1-3] Most prior DIB studies employed organic solvents or ionic liquids (ILs) for the electrolytes.^[4-6] Recently, DIBs that employ aqueous electrolytes have engendered attention due to the inherent advantages of safety and cost. The primary challenge of DIBs comes from the anion-insertion reactions in the cathode materials. Graphite remains a competitive cathode candidate for aqueous DIBs regarding the cost and scalability.^[7-13]

However, the anion intercalation potential of graphite can be high enough to electrolyze aqueous electrolytes, where the oxygen evolution reaction (OER) transpires before the anion-insertion. To tackle the problem, one approach is to use water-in-salt electrolytes (WiSE) or deep eutectic solvents (DES) as electrolytes. According to the Nernstian relationship, the low activity of water enhances the anodic stability of water as all water is bound as ligand, and the high anion activity lowers its insertion potential.^[3,5,14-20]

As for anion charge carriers, superhalides are promising (**Table S1**). For example, the insertion of $[\text{AlCl}_4]^-$ into graphite has been widely investigated from ionic liquid electrolytes.^[21-25] Recently, our group demonstrated that graphite can reversibly host $[\text{MgCl}_3]^-$, another superhalide, with a reversible capacity of 151 mAh g^{-1} from a concentrated aqueous DES electrolyte that comprises 9 *m* (moles per kg of solvent) MgCl_2 and 30 *m* choline chloride (ChCl).^[20] Compared to $[\text{AlCl}_4]^-$, $[\text{MgCl}_3]^-$ is lighter; along this line, it is intriguing to learn whether graphite can store an even lighter and smaller superchloride of $[\text{LiCl}_2]^-$ with the interests of enhanced reversibility and cycling performance.^[26,27]

To date, $[\text{LiCl}_2]^-$ has only been only observed by photoelectron spectroscopy as a high-voltage-induced anion from 0.0001 M LiCl solvated in a water/methanol mixture.^[26] Herein, we found in a DES electrolyte of 20 *m* LiCl + 20 *m* ChCl , $[\text{LiCl}_2]^-$ is the major anionic species, as shown by the femtosecond stimulated Raman spectroscopy (FSRS) results. In this electrolyte, graphite cathode exhibits a reversible anion-storage capacity around 110 mAh g^{-1} over 400

cycles. Our ^7Li and ^2H magic angle spinning nuclear magnetic resonance (MAS-NMR) results suggest that hydrated $[\text{LiCl}_2]^-$ is inserted in graphite, which is supported by the density function theory (DFT) calculations.

2. Results and Discussion

FSRS experiments were conducted to investigate whether $[\text{LiCl}_2]^-$ forms in the working electrolytes.^[28] The speciation of Li–Cl can be reflected by the O–H stretching and H–O–H bending modes of the surrounding water molecules. **Figure 1a** displays the ground-state FSRS spectra of water O–H stretching mode in a series of solutions. Notable changes in 20 *m* LiCl are the reduced signal at $\sim 3200\text{ cm}^{-1}$ and a blue-shifted and enhanced peak above 3400 cm^{-1} compared to pure water. These two peaks are characteristic of the more hydrogen (H)-bonded and less H-bonded configurations of water molecules, respectively. The results thus suggest that the original H-bonding network in bulk water is disrupted in electrolytes, where water molecules coordinate a strong Lewis acid of Li^+ (**Figure 1c,e,f**).^[29–33] Similar phenomenon was also observed in concentrated ZnCl_2 electrolytes.^[16] In 20 *m* ChCl , the relative intensity for the $\sim 3200\text{ cm}^{-1}$ peak is also reduced compared to pure water, but to a lesser extent for the 3400 cm^{-1} peak, wherein a small redshift is observed with LiCl concentration increase. Interestingly, in the mixed electrolytes comprising different concentrations of LiCl and 20 *m* ChCl , the spectra largely resemble that of 20 *m* ChCl . This finding suggests that the primary cation in the mixed electrolyte of (LiCl + ChCl) is Ch^+ , instead of Li^+ , where Li^+ cannot interact with water molecules directly or fully because Li^+ is coordinated by the excessive chloride ions, a stronger Lewis base than water. The gradual increase of the $\sim 3400\text{ cm}^{-1}$ peak with 5 *m* LiCl, 10 *m* LiCl, and 20 *m* LiCl in the presence of 20 *m* ChCl reflects larger polarizability of water stretching mode in proximity to Li^+ instead of only Ch^+ .

The bending mode of water molecules is rarely conspicuous in Raman studies due to its much weaker intensity and broad bandwidth.^[34] However, the water bending mode displays a clear change pattern as a function of varying concentrations of LiCl added to 20 *m* ChCl (**Figure 1b**). Notably, the water spectrum has been subtracted from the spectra of electrolytes; therefore, the spectra in **Figure 1b** represent the changes of water bending mode due to interaction with electrolytes. First, only one peak at 1650 cm^{-1} appears for 20 *m* LiCl, which can be assigned to $[\text{Li}(\text{H}_2\text{O})_3\text{Cl}]$ (**Figure 1c**).^[31,33] The bending mode of water barely exhibits a change in 20 *m* ChCl , where its spectrum serves as a background to examine the ground-state FSRS signal-to-noise ratio. Upon the addition of 5 *m* LiCl to 20 *m* ChCl , we observed a clear emerging broad band around 1678 cm^{-1} , which can be assigned to $[\text{LiCl}_4]^{3-}$ (**Figure 1d**). When 10 *m* LiCl is

added, the peak around 1663 cm^{-1} rises, likely due to the formation of $[\text{Li}(\text{H}_2\text{O})\text{Cl}_3]^{2-}$, consistent with the Li:Cl ratio of 1:3 (**Figure 1e**). Lastly, in $20\text{ m ChCl} + 20\text{ m LiCl}$, a broad peak emerges in a range of $1650\text{--}1660\text{ cm}^{-1}$, which corresponds to $[\text{Li}(\text{H}_2\text{O})_2\text{Cl}_2]^-$, a superhalide, and is consistent with the Li:Cl ratio of 1:2 (**Figure 1f**). Note that quantum optimizations were conducted to understand these electrolyte structures. Such DFT calculations have been used and validated by Zn^{2+} and Mg^{2+} containing species in water-in-salt electrolytes.^[16,20] Interestingly, the Raman spectrum of $25\text{ m LiCl} + 25\text{ m ChCl}$ compared to that of $20\text{ m LiCl} + 20\text{ m ChCl}$ demonstrates a change in the coordination environment and a decrease in the water bending peak intensity (**Figure S1**).

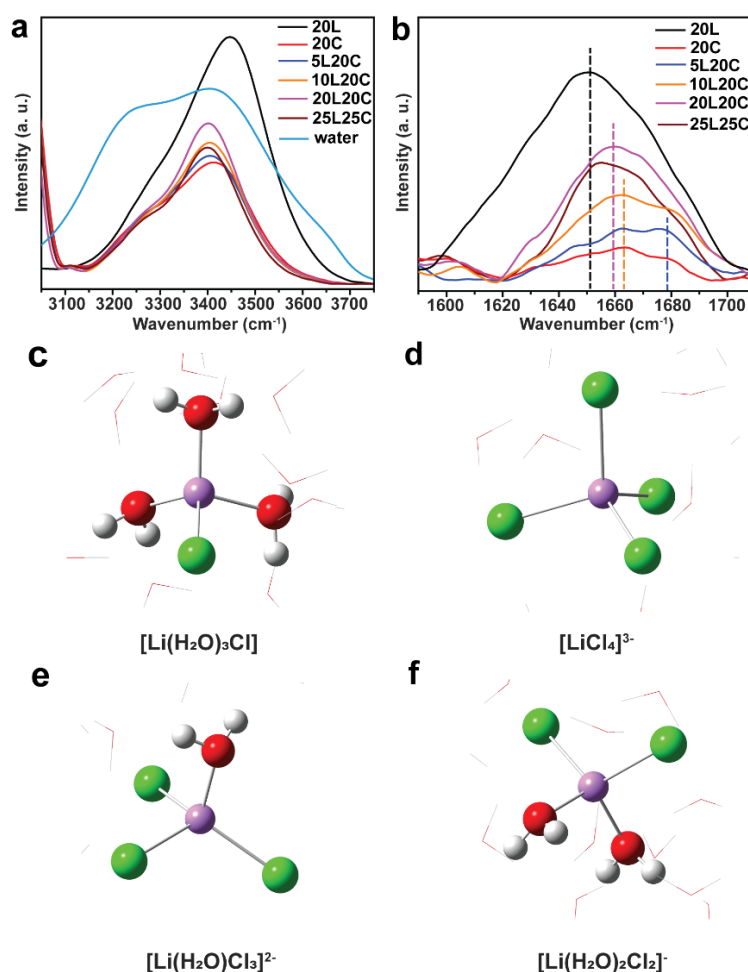


Figure 1. Stimulated Raman spectra of 20 m LiCl (20L), 20 m ChCl (20C), and the mixed electrolytes, $5\text{ m LiCl} + 20\text{ m ChCl}$ (5L20C), $10\text{ m LiCl} + 20\text{ m ChCl}$ (10L20C), $20\text{ m LiCl} + 20\text{ m ChCl}$ (20L20C), $25\text{ m LiCl} + 25\text{ m ChCl}$ (25L25C) for (a) O–H stretching mode of water (ca. $3000\text{--}3800\text{ cm}^{-1}$), and (b) H–O–H bending mode of water (ca. $1590\text{--}1710\text{ cm}^{-1}$). Major peaks for H–O–H bending mode are denoted by dashed lines with the corresponding color for each sample solution spectrum. Calculated structures of stabilized complex ions in the electrolytes: (c) $[\text{Li}(\text{H}_2\text{O})_3\text{Cl}]$ (20L and 25L25C); (d) $[\text{LiCl}_4]^{3-}$ (5L20C); (e) $[\text{Li}(\text{H}_2\text{O})\text{Cl}_3]^{2-}$ (10L20C); and (f) $[\text{Li}(\text{H}_2\text{O})_2\text{Cl}_2]^-$ (20L20C).

The major peak shifts closer to 1650 cm^{-1} , which suggests that $[\text{Li}(\text{H}_2\text{O})_3\text{Cl}]$ becomes a major species in concentrated $25\text{ m LiCl} + 25\text{ m ChCl}$, releasing some of the chloride that is tied up at 20 m , resulting in free chloride in this mixture. This type of systematic spectral observation confirms that the polarizability of water bending mode changes more with the cation Li^+ than the anion Cl^- , and the observed Raman peak can be attributed to characteristic bending motions of water molecules coordinated and/or perturbed by the electrolytes, not the non-interacting bulk water molecules.^[30,35]

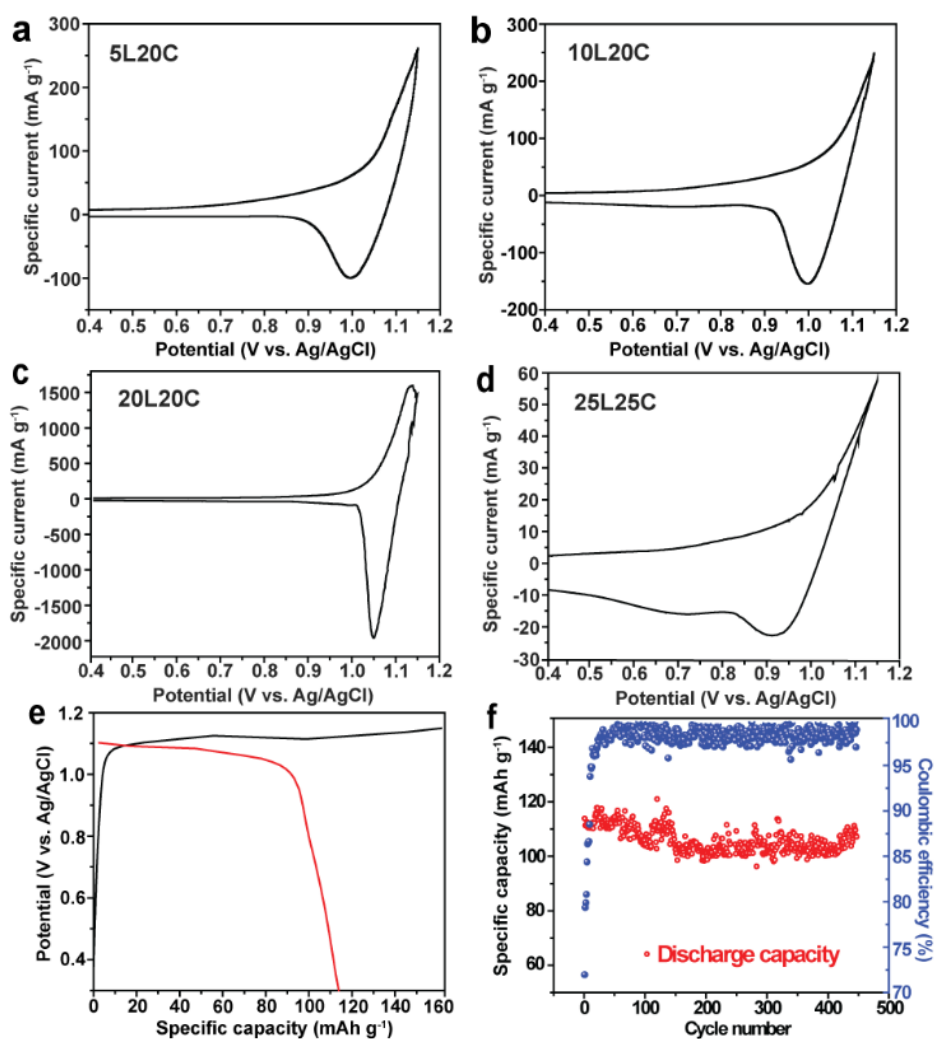


Figure 2. Electrochemical characterization of graphite electrode in different electrolytes. CV curves of (a) 5L20C, (b) 10L20C, (c) 20L20C, and (d) 25L25C at a scan rate of 0.1 mV s^{-1} . Note the vastly different ordinate scales in plots (a-d). (e) the 1st cycle GCD profiles and (f) the cycling performance of graphite in 20L20C at a current rate of 50 mA g^{-1} in a potential window from 0.3 to 1.15 V.

We conducted cyclic voltammetry (CV) to evaluate the anion storage properties in the graphite electrode from the above electrolytes at a scan rate of 0.1 mV s^{-1} (Figure 2a-d). In

5L20C and 10L20C, the upper cutoff potential of 1.15 V (vs. Ag/AgCl, hereafter, unless specified) was reached prior to arriving at the apex of the anodic current. In contrast, in 20L20C, the anodic current peak was observed at 1.14 V, where the polarization was only 0.085 V with the cathodic current peaked at 1.05 V, a higher potential than those in 5L20C and 10L20C. Note that 20L20C showed the smallest degree of polarization despite its highest viscosity among the three electrolytes investigated. This discrepancy may relate to the insertion of different anionic charge carriers. As suggested by the FSRS results, it is reasonable that the insertion of monovalent $[\text{Li}(\text{H}_2\text{O})_2\text{Cl}_2]^-$ or dehydrated $[\text{LiCl}_2]^-$ possesses faster kinetics than the insertion of divalent $[\text{Li}(\text{H}_2\text{O})\text{Cl}_3]^{2-}$ and trivalent $[\text{LiCl}_4]^{3-}$. Interestingly, when the concentration became even higher in 25L25C, the specific current in CV curves plummets to 0.013% of that in 20L20C, which indicates the absence of sufficient anion charge carriers that can be inserted into graphite (**Figure 2d**). Calculated from the CV results, different electrolytes exhibit vastly different Coulombic efficiency (CE) for the anion hosting in graphite, where the CE is 22.8%, 40.4%, 78.3%, and 41.7% in 5L20C, 10L20C, 20L20C, and 25L25C, respectively.

In light of the more reversible electrochemical properties associated with the $[\text{LiCl}_2]^-$ as the charge carrier, our further studies focused on the electrolyte of 20L20C. **Figure 2e** shows the first cycle Galvanostatic charge-discharge (GCD) potential profiles of graphite in 20L20C at a current rate of 50 mA g⁻¹. The first charge and discharge processes deliver capacity values of 158 mAh g⁻¹ and 114 mAh g⁻¹, respectively. The initial discharge capacity indicates that each inserted $[\text{LiCl}_2]^-$ corresponds to 20 carbon atoms in the intercalation compound. Due to the activation of the structure during the initial cycles as well as parasitic reactions of electrolytes on the surface of the electrode, the insertion/deinsertion of Li-Cl superhalides exhibits a low initial CE of 72.2 %, where a similar phenomenon was also observed in the reversible storage of Mg-Cl superhalides in graphite. After 10 cycles, the CE rises to 93.9%, which is stabilized during the next 437 cycles with an average CE of 98.4% (**Figure 2f**). The capacity retention of graphite in 20L20C is significantly improved compared to the storage of $[\text{MgCl}_3]^-$, where the capacity retention is 94.2% after 440 cycles in contrast to 48.6% after 300 cycles for $[\text{MgCl}_3]^-$.^[20] We tentatively attribute the better cycling results to the structural compactness of $[\text{LiCl}_2]^-$ as a charge carrier, which causes less strain to graphite structure than $[\text{MgCl}_3]^-$. Note that graphite electrode exhibits a moderate rate performance for the storage of compact $[\text{LiCl}_2]^-$ when varying current rates are applied (**Figure S2**). It is not clear whether the water co-insertion helps retain the graphite structure, where its benefits should not be ruled out.

Having established hydrated $[\text{LiCl}_2]^-$ as dominant in the electrolyte, we investigated whether $[\text{LiCl}_2]^-$ is also the charge carrier inserted in graphite. The first question is whether

chloride can be reversibly inserted into graphite from its concentrated electrolytes. Our prior studies have demonstrated that from concentrated ChCl (30 *m*), chloride ions cannot be inserted into graphite.^[20] Here, we further tested concentrated 20 *m* LiCl (20L) and 40 *m* ChCl (40C) as the electrolytes attempting for oxidative insertion of chloride into graphite. Based on the Nernst equation, the theoretical chlorine evolution reaction (CER) onset potential values are 1.08 V and 1.06 V for 20L and 40C, respectively. Indeed, irreversible CER takes place in these electrolytes upon the initial charge, as shown by the GCD profiles (**Figure S3a,c**); the following discharge exhibits a negligible capacity of ~20 mAh g⁻¹, where CE values are less than 1%. The CV curves also demonstrate the low CE due to the prevailing CER in 20L and 40C (**Figure S3b,d**). The disparity in redox behaviors between these electrolytes and 20L20C suggests that the active charge carrier inserted into graphite from 20L20C cannot be Cl⁻ solely.

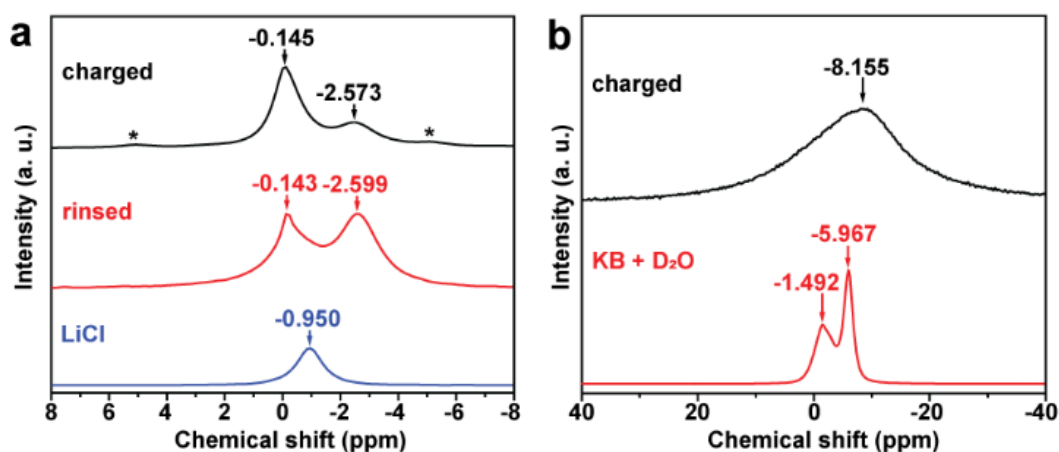


Figure 3. (a) ⁷Li MAS NMR spectra of the charged graphite electrode (black); the charged graphite electrode after rinsing with DMSO (red); and LiCl solid (blue). Spinning side bands for the charged graphite electrode before rinsing is marked with *. (b) ²H static-NMR spectra of the charged graphite electrode (black) and the charged KB electrode (red), where D₂O was used as a solvent.

Inductively coupled plasma mass spectrometry (ICP-MS) reveals the elemental makeup and stoichiometry of the charged graphite electrode at different state of charge (SOC) cycled in 20L20C (**Table S2**). At the completion of the first charge, where anions are oxidatively inserted into graphite, a molar ratio between Cl⁻ and Li⁺ is 2.3±0.1. This ratio suggests that the inserted charge carrier is [LiCl₂]⁻ or hydrated [LiCl₂]⁻. The molar ratio of Cl⁻ to Li⁺ in the electrode upon the first discharge is measured as 4.5±0.3, which indicates that some chloride ions remain trapped in the structure upon the first charge, being responsible for the low initial CE of ~ 71 % in the first cycle of GCD.

To understand the chemical environment inside the charged graphite electrode, we collected spectra of ^7Li magic angle spinning nuclear magnetic resonance (MAS NMR). For the charged electrode, rinsing the electrode by dimethyl sulfoxide (DMSO) removes the electrolyte residue, which is reflected by the ^7Li MAS NMR spectra. As **Figure 3a** illustrates, upon rinsing, the narrower peak at ca. -0.14 ppm assigned to Li^+ from the electrolyte residue diminishes, and the relative peak intensity around -2.6 ppm is increased, which can be attributed to the inserted Li-ions in the graphite electrode. The -2.6 ppm peak is much broader than the -0.14 ppm peak, which reflecting the slower motion of the inserted Li-ions. This peak shift at ca. -2.6 ppm belongs to neither Knight shift (e.g., 41-44 ppm for LiC_6 or LiC_{12} and 5-10 ppm for LiC_x , where $x \geq 18$), nor paramagnetic shift (e.g., 260 ppm for LiCoO_2).^[36,37] Negative peak shift in ^7Li NMR has been observed from anion-coordinated Li-ions in organic solvents (e.g., LiPF_6 or LiTFSI in carbonate electrolytes), but not from inserted Li^+ in graphite, which can be ascribed to stronger shielding effect on Li^+ coordinated by two Cl^- in our case.^[38,39] The more negative shift of ^7Li NMR compared to that of solid LiCl at -0.950 ppm reveals a higher electron density around the inserted Li^+ , which supports the insertion of Li-containing superhalide into graphite.

An important question is whether aqua-ligands are co-inserted into graphite during charging. To address this point, we collected the ^2H static-NMR spectrum of the charged graphite electrode in deuterated 20L20C as the electrolyte, which displays one broad peak with a chemical shift at -8.155 ppm (**Fig 3b**). The following question is whether the signal comes from water co-inserted into graphite's galleries or from water adsorbed by the carbon additive KetjenBlack (KB), which is present in the electrode to enhance electronic conductivity. As a control experiment, we collected another ^2H NMR spectrum of D_2O in a pure KB electrode that was charged to the same cutoff potential. The chemical shift observed with D_2O in KB shows two sharp peaks (-5.967 and -1.194 ppm) and does not coincide with the shifts of the charged graphite electrode; no broad components appeared in the spectrum even in the scanning over 2600 times. Therefore, the broad peak with characteristic chemical shift of the charged graphite can be assigned to the deuterated water co-intercalated in the graphite structure. The intercalated water seems to exhibit almost free isotropic rotation, reflected by the narrow peak width (ca. 3 kHz); however, it is still broader than the width of bulk D_2O liquid signal.

We performed a set of higher-level DFT calculations to analyze the structures and energies of possible geometries with Li-Cl anions inserted in a graphene bilayer. Particularly, the purpose of computational analysis was to predict whether it is favorable for water to be co-intercalated with $[\text{LiCl}_2]^-$, and if so, whether water remains bound to $[\text{LiCl}_2]^-$ after insertion. **Figure 4** shows the relaxed geometry of six potential bi-layered graphite intercalation

compounds (GICs): one for $[\text{LiCl}_2]^-$ inserted without water, two for inserted $[\text{LiCl}_2]^-$ bound to a single water molecule, and three for $[\text{LiCl}_2]^-$ that remains bound to two H_2O molecules. All these structures are charge neutral. The size of these compute cells and the bilayer geometry were chosen to minimize interactions between ions either in the same gallery or in adjacent galleries; however, ion loading is equivalent to 71 mAh g^{-1} in bulk graphite, or around two-thirds of the experimental measured reversible capacity. For each geometry, we evaluated the voltage for insertion (ΔV_{e^-}) of these structures using the equation below:

$$\Delta V_{e^-} = (E_{\text{GIC}} + \Delta n E_{\text{H}_2\text{O}}) - (E_{\text{gr}} + E_{[\text{Li}(\text{H}_2\text{O})_{2-n}\text{Cl}_2]^-}) \quad (1)$$

where, E_{GIC} , E_{gr} , and $E_{[\text{Li}(\text{H}_2\text{O})_{2-n}\text{Cl}_2]^-}$ ($n = 0, 1, 2$) denote the total energy of relaxed GIC, empty graphene, and the hydrated $[\text{LiCl}_2]^-$ anion, respectively. Δn is the number of water molecules that were stripped off $[\text{Li}(\text{H}_2\text{O})_2\text{Cl}_2]^-$ and left in the electrolyte during insertion, and $E_{\text{H}_2\text{O}}$ is the energy of an H_2O molecule in water (the energy of any water that was left behind prior to anion insertion).

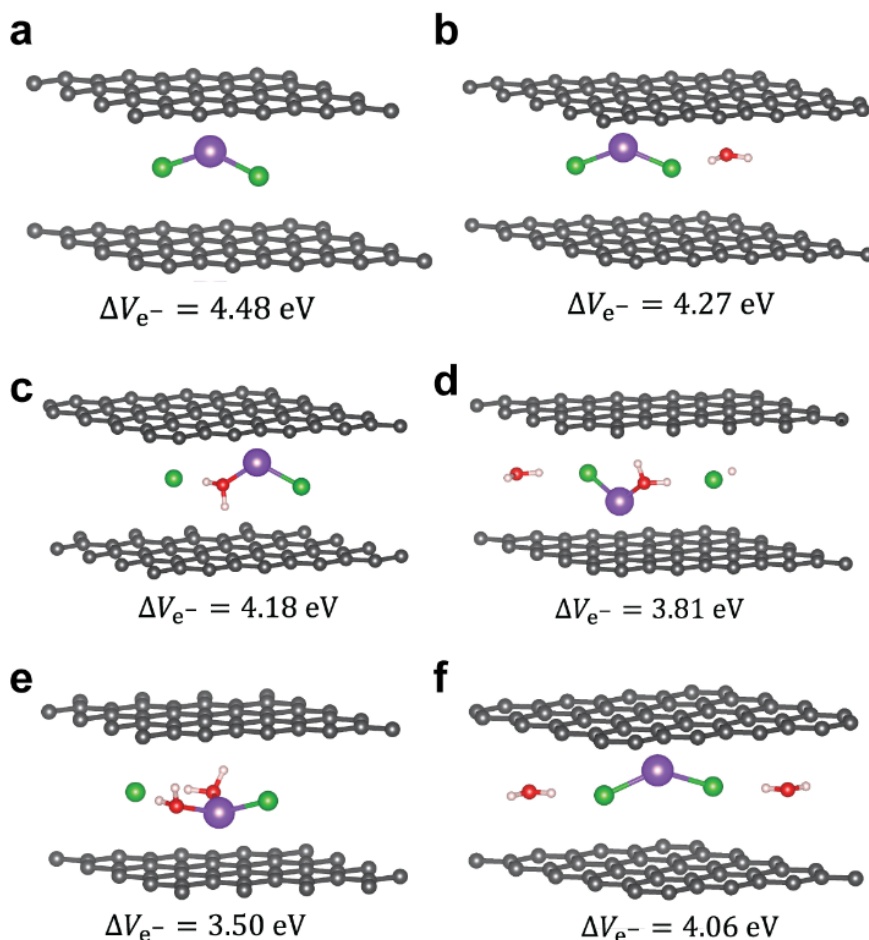


Figure 4. Relaxed atomic structures of anion-inserted bi-layered graphene with (a) $[\text{LiCl}_2]^-$, (b) $[\text{Li}(\text{H}_2\text{O})\text{Cl}_2]^-$ (A), (c) $[\text{Li}(\text{H}_2\text{O})\text{Cl}_2]^-$ (B), (d) $[\text{Li}(\text{H}_2\text{O})_2\text{Cl}_2]^-$ (A), (e) $[\text{Li}(\text{H}_2\text{O})_2\text{Cl}_2]^-$ (B), and (f) $[\text{Li}(\text{H}_2\text{O})_2\text{Cl}_2]^-$ (C). Insertion voltage values (ΔV_{e^-}) are annotated for the structures.

From the calculations, the hydrated anion-insertion potentials are lower, that is, the insertion of hydrated $[\text{LiCl}_2]^-$ with two water molecules is more favorable, which corroborates the NMR results. In all of the low energy structures the co-intercalated water is only one or two-fold coordinated leaving it relatively free to rotate, consistent with the NMR observations. Moreover, in the lowest energy structure one of the chloride ions becomes loosely bound to the Li through the water and may be the origin of some Cl being left in the graphite in the first few charging cycles.

To determine the counter charge that is distributed when the anion is inserted, we have computed the electronic charge transfer between the intercalated compounds and graphite by calculating the electron density difference ($\Delta\rho$) using the equation,

$$\Delta\rho = \rho_{\text{GIC}} - \rho_{\text{gr}^+} - \rho_{[\text{Li}(\text{H}_2\text{O})_n\text{Cl}_2]^-} \quad (2)$$

where ρ_{GIC} , ρ_{gr} , and $\rho_{[\text{Li}(\text{H}_2\text{O})_n\text{Cl}_2]^-}$ ($n = 0$ or $n = 2$) are the charge density of the GIC, bi-layered graphene with a positive charge, and the intercalated species with a negative charge, respectively. In the charge density difference maps for the GIC structure with $[\text{LiCl}_2]^-$ or $[\text{Li}(\text{H}_2\text{O})_2\text{Cl}_2]^-$ (B) inserted in positively charged bi-layered graphene conformation (**Figure 5**), blue and yellow shades show the regions with electron loss and gain, respectively.

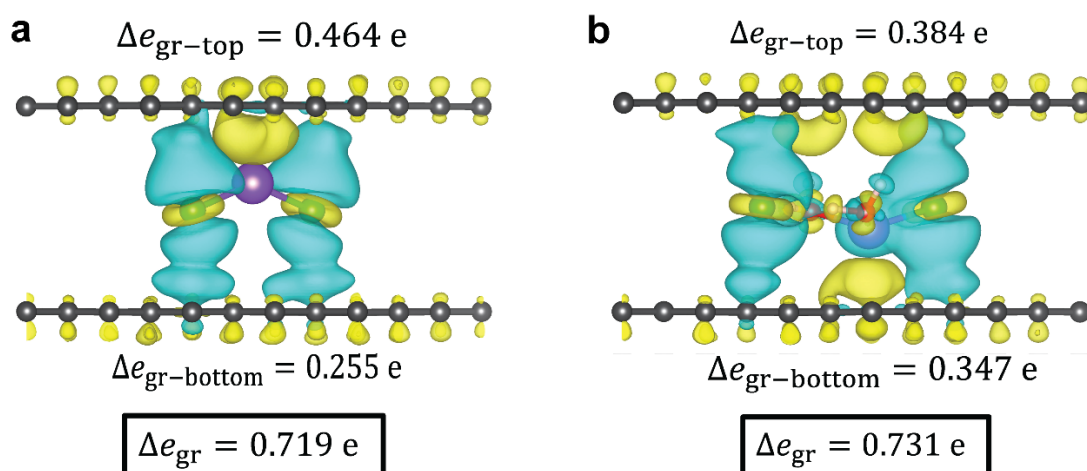


Figure 5. Electron density difference maps for (a) $[\text{LiCl}_2]^-$ in positively charged bi-layered graphene, and (b) $[\text{Li}(\text{H}_2\text{O})_2\text{Cl}_2]^-$ (B) in positively charged bi-layered graphene. Blue and yellow areas indicate

the electron loss and gain, respectively, as a result of intercalation. An isosurface value of 0.001 was used for the plots. Δe_{gr} , Δe_{gr-top} , and $\Delta e_{gr-bottom}$ show the net charge on the graphene bilayer, top layer, and bottom layer, respectively.

In the $[\text{LiCl}_2]^-$ inserted bi-layered graphene, regions with electron loss are observed above the bottom graphene layer, while in the region below the top layer both electron loss and gain regions are observed (**Figure 5a**). In contrast, in the $[\text{Li}(\text{H}_2\text{O})_2\text{Cl}_2]^-$ (B) inserted structure, a more homogeneous charge distribution across the interface is apparent, with electron loss and gain regions observed at the interface of both layers (**Figure 5b**). The Bader charge analysis (annotated in **Figure 5**) indicates that the bulk of the inserted anion's charge is transferred to graphite, with the majority transferred to the graphene sheet closest to Li^+ . This charge transfer is slightly larger when the solo anion is intercalated, but it is more equitably distributed between both graphene sheets when the anion is co-inserted with water. For insertion of Na-ions in graphite, it has been reported that solvent co-insertion causes an increase in its insertion potential due to lowered desolvation energy. The co-inserted solvent screens the charge of the intercalant Na-ion, which weakens the interaction of the cations with the host materials, where stable cycling life was observed.^[40] Similarly, the solvated anions are expected to be strongly bound to the solvent molecules more than the host materials. This screening effect of water molecules may be beneficial for inserting anions in graphite for better cycling stability. To summarize, water molecules may invoke a screening effect that benefits the hosting of complex anions by graphite, resulting in a lower insertion potential of hydrated Li-Cl superhalides and the formation of a more stable GIC.

We have also performed calculations of pairs of $[\text{Li}(\text{H}_2\text{O})_2\text{Cl}_2]^-$ ions with configuration (B) inserted into bilayer graphene at a density equivalent to the full capacity of 114 mAh g⁻¹ measured experimentally, the results of which are shown in the SI (**Figure S6**). The geometry of these calculations was set up to permit the ions to interact. With this freedom, the ions coordinate with one another through the water forming a 2D crystalline intercalation compound for which the insertion energy per ion is 0.50 eV more favorable than for the non-interacting ions.

Hydrated $[\text{LiCl}_2]^-$ is larger than K^+ in radii. It is expected that the insertion of hydrated $[\text{LiCl}_2]^-$ in graphite could cause a larger volume expansion of the graphite structure than that from graphite to the stage-I GIC of KC_8 . Note that from graphite to KC_8 , the volume of the graphite host expands 61%, theoretically. In our prior work, we reported that the storage of Mg-Cl superhalides does not form long-range ordered acceptor-type GIC. To understand whether

the storage Li-Cl superhalides induces similar structural transformation of graphite, we collectively analyzed data from *ex situ* XRD, spontaneous Raman spectra, and *ex situ* high-resolution transmission electron microscopy (HRTEM) at different SOC of the graphite electrode: pristine, fully charged, and fully discharged. No new diffraction peaks for a GIC were observed on the charged or discharged graphite electrode. Instead, the (002) peak intensity was clearly decreased due to the reduced crystallinity of graphite (**Figure S4**). To understand whether cycling continuously damages the structure of the graphite electrode, we collected *ex situ* XRD patterns of the electrode upon the completion of the 300th cycle. As shown in **Figure S4**, the (002) peak of the graphite's layered structure does not show a significant reduction from the completion of the 1st to the 300th cycle. This concludes that the distortion of the structure primarily comes from the initial insertion of Li-Cl superhalides, where a drastic decrease in the (002) peak intensity took place after the 1st cycle. Once this activation process is completed, following cycling does not further lower the crystallinity of graphite. Moreover, the Raman spectra of the graphite electrode at different SOC (**Figure S5**) unequivocally supports XRD results in terms of the creation of defective sites upon cycling, where the G/D ratio decreased from 5.09 (pristine) to 2.07 (charged). HRTEM images show that the insertion of Li-Cl superhalides renders the graphite structure turbostratic, and the de-insertion does not restore the long-range order of graphite (**Figure 6**).

3. Conclusions

In summary, we report the presence of $[\text{LiCl}_2]^-$ in a DES of 20 *m* LiCl and 20 *m* ChCl that serves as the charge carrier for the anodic insertion in graphite as a cathode in DIBs. The storage of $[\text{LiCl}_2]^-$ in graphite leads to a capacity of $\sim 110 \text{ mAh g}^{-1}$ that is stable during a long cycle life of over 440 cycles. The integrated spectroscopic characterization with FSRS, MAS NMR, and DFT calculations support the notion that hydrated $[\text{LiCl}_2]^-$ are inserted into graphite. Structural characterization reveals that the insertion of $[\text{LiCl}_2]^-$ in graphite turns the structure turbostratic. Although the combination of the graphite cathode and an aqueous electrolyte does not confer a high Coulombic efficiency, this study reveals that it is viable to use the smallest and lightest superchloride as the charge carrier for DIBs in aqueous electrolytes. More intriguingly, water molecules can be co-inserted into graphite, which points to a viable synthetic route by electrochemistry for water-GICs.

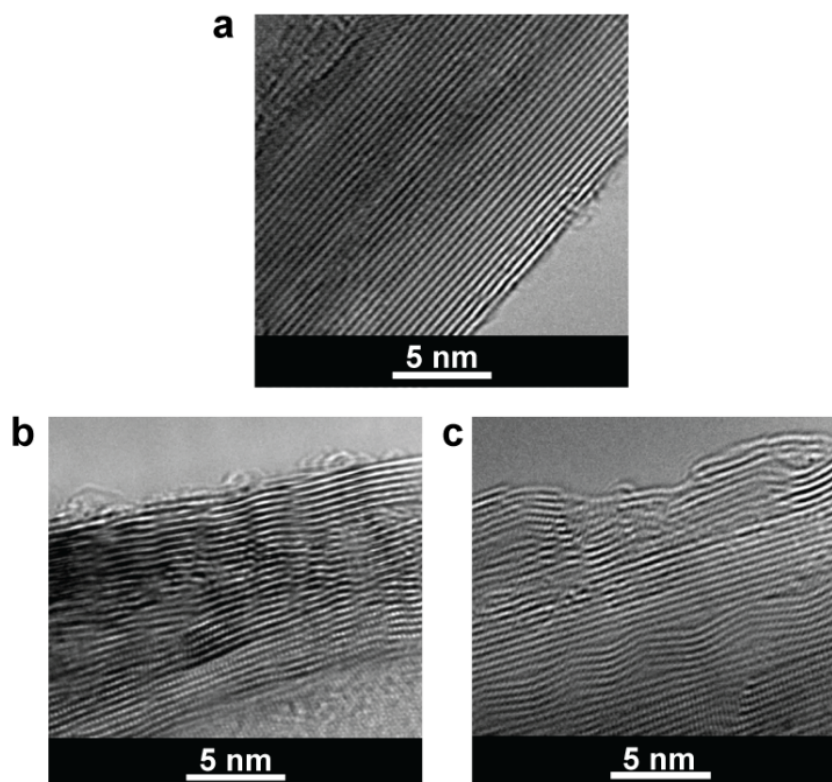


Figure 6. HRTEM images of graphite electrodes at different SOC. (a) pristine; (b) fully-charged; and (c) fully-discharged.

4. Experimental Section/Methods

Material preparation: Both counter (activated carbon, AC) and working (1 micron particle size graphite) electrodes were prepared in free-standing films. The electrodes comprise active material, conductive carbon additives, and polytetrafluoroethylene (PTFE) binder with a mass ratio 7:2:1, unless specified. Graphite working electrodes for structural characterization were composed of 80 wt.% graphite and 20 wt.% PTFE binder. Average active mass loading was 2.5 mg cm^{-2} . All electrolyte samples were prepared by mixing the designated molality of salts; lithium chloride (LiCl, anhydrous, $\geq 98\%$, Sigma Aldrich) and choline chloride (ChCl, TCI) with de-ionized water, which were then kept under 80°C overnight to form transparent solution.

Electrochemical measurements: A three-electrode Swagelok[®] cell setup was used with AC as the counter electrode, the Ag/AgCl reference electrode ($E = 0.230$ vs. Standard Hydrogen Electrode, SHE), and the composite working electrode. The cyclic voltammetry (CV) was conducted on Biologic VMP-3 with a scan rate of 0.1 mV s^{-1} . Galvanostatic charge/discharge (GCD) measurements were performed on a Landt CT3001A cell tester at 50 mA g^{-1} , unless specified.

GS-FSRS measurements: Our FSRS setup has been based on an ultrafast laser regenerative amplifier (Legend Elite-USP-1K-HE, Coherent, Inc.) seeded by a mode-locked Ti:Sapphire oscillator (Mantis-5, Coherent, Inc.), which generated the fundamental pulse train with 1 kHz repetition rate, ~800 nm center wavelength, ~35 femtosecond (fs) pulse duration, and ~3.7 W average power. For the electronic ground state (GS)-FSRS measurement, the picosecond (ps) Raman pump pulse was produced through a three-part home-built system: (i) a fs noncollinear optical parametric amplifier (NOPA) generated a tunable fs seed, which was then stretched to ps duration by a grating-slit-based spectral filter, (ii) a second harmonic bandwidth compressor (SHBC) produced a ps 400 nm pump pulse, and (iii) a two-stage ps-NOPA system amplified the ps seed by the ps 400 nm pump to the desired power. The Raman pump used in this experiment was tuned to 510 nm wavelength with ~2 mW power.^[28,41]

For the broadband Raman probe, a supercontinuum white light (SCWL) was generated by irradiating a small portion of the 800 nm fundamental pulse through a 2-mm-thick de-ionized water-filled quartz cuvette (Spectrosil 1-Q-2, Starna Cells). The transmitted probe was then compressed by a chirped mirror pair (DCM-9, 450–950 nm, Laser Quantum, Inc.) to ~100 fs pulse duration.^[42] The incident Raman pump and probe pulses were focused by a parabolic reflective mirror onto a 1-mm-thick quartz cell filled with the sample electrolyte solution. The pump was then blocked by a pinhole after the cell while the probe was spatially dispersed via a reflective grating (500 nm blaze wavelength, 600 groves/mm) inside a spectrograph (IsoPlane SCT-320, Princeton Instruments, Inc.) and imaged on a front-illuminated CCD array camera (PIXIS:100F, Princeton Instruments, Inc.).

For the water H–O–H bending region (ca. 1500 to 1800 cm^{-1}), the Raman spectrum of pure water was subtracted from the spectra of the sample solutions, then a smooth baseline was drawn. For the water O–H stretching region (ca. 3000 to 4000 cm^{-1}) of the electrolyte samples, no pure water spectrum was deducted.^[43] All the spectroscopic measurements were conducted at room temperature (~22 °C).

Quantum optimization of electrolyte structures: The structural optimization of various electrolytes was performed in Gaussian 16 software with density functional theory (DFT) method and RB3LYP functional.^[44] All the $[\text{Li}(\text{H}_2\text{O})_x\text{Cl}_{4-x}]^{x-3}$ ($x=0$ to 4) complexes were constructed with a tetrahedral geometry based on literature, and a solvation shell with 18 water molecules was randomly added around the complexes.^[45,46] The bulk water was modeled by the default integral equation formalism polarizable continuum model (IEFPCM). The structures were first optimized with 3-21G then 6-31G basis sets.^[47] The 6-31G(d,p) basis sets were used for $[\text{Li}(\text{H}_2\text{O})_4]^+$ and $[\text{Li}(\text{H}_2\text{O})_3\text{Cl}]$ due to their positive and neutral charge, while the diffuse

function was added for heavy atoms on $[\text{Li}(\text{H}_2\text{O})_2\text{Cl}_2]^-$, $[\text{Li}(\text{H}_2\text{O})\text{Cl}_3]^{2-}$, and $[\text{LiCl}_4]^{3-}$ because of the negative charge. No imaginary frequency was observed for the optimized structures (see **Figure 1c-f** in main text).

ICP-MS measurements: Graphite electrode samples were weighed out and leached in 6 mL of 8 M (“charged”) or 13 M (“discharged”) ultrapure nitric acid (Aristar Ultra grade, BDH Chemical). After a period of ≥ 4 days the leaches were diluted for analysis. Lithium and Cl concentrations were determined by external calibration using a Spectro Arcos ICP-OES with the torch mounted in End-On Position, at the W.M. Keck Collaboratory for Plasma Mass Spectrometry at Oregon State University.

NMR measurements: The ^7Li MAS NMR and ^2H static NMR measurements were performed using an NMR system consisting of a 11.7 T magnet and a spectrometer (DD2; Agilent Technologies Inc.). For ^7Li measurement, a cycled electrode was picked up from a Swagelok® T-cell. The electrode was rinsed by dimethyl sulfoxide (DMSO, Sigma Aldrich), then ground and mixed with polymer (PVdF) powder with a volume ratio 1:3 using an agate mortar. The mixed powder was put in a MAS rotor (3.2 mm ϕ). The ^7Li MAS NMR spectra were measured by 5–10 kHz spinning speed using a single pulse sequence with a 2.5 μs pulse and 10 s pulse delay. For ^2H static NMR, a cycled electrode prepared using deuterated water (D_2O) solvent instead of water solvent was picked up from the cell and wiped gently, and then sealed in a glass tube (9 mm ϕ). The sample was measured by applying a quadrupole echo pulse sequence with 6 μs (90°x , 90°y) pulses. As a reference, a mixed sample of Ketjenblack (KB) and D_2O was also measured. 1 M LiCl aqueous solution and D_2O were used as chemical shift references (0 ppm) of ^7Li and ^2H , respectively.

Higher-level DFT calculations: Density Functional Theory (DFT) calculations were performed using the projected augmented wave (PAW) basis set as implemented in the Vienna Ab initio Simulation Package (VASP).^[48-50] For these calculations, the plane-wave-pseudopotentials based on with the Perdew-Burke-Ernzerhof (PBE) exchange correlation functional and generalized gradient approximation (GGA) correction were employed.^[51] For the molecules and GICs, it was found that sampling the Brillouin zone with a $1 \times 1 \times 1$ Gamma-centered k-point grid was sufficient to fully converge the computed insertion energies. The cutoff energy was 520 eV, and the structures were optimized to minimize the forces on ions to equal or be better than 0.01 eV. For the solvated molecules, we used the VASP implicit solvation calculations.^[52] To quantify the charge transfer between the graphene and intercalated compounds we used Bader charge analysis.^[53]

Other characterization of electrodes: Electrodes for physical characterization were prepared without conductive carbon additive, i.e., KetjenBlack. DMSO was employed as the rinsing agent. Rigaku Ultima IV was employed to obtain the X-ray diffraction (XRD) patterns of electrodes (Cu K α radiation, $\lambda = 1.5406 \text{ \AA}$). The spontaneous Raman spectra of electrodes were collected on a WITec alpha300 confocal Raman microscope with a continuous-wave 514 nm Ar-ion laser source. High-resolution transmission electron microscopy (HRTEM) images for structural transformation on the electrodes were taken using Titan 80-300 HRTEM. The atomic composition of elements on electrode samples was obtained by FEI Quanta 600F Field Emission Environmental SEM with an insertable backscatter and Cathode Luminescence.

SI calculations: Same approach was taken for CE calculation from CV curves, theoretical onset potential of CER and OER from our previous work.^[20]

Supporting Information

Supporting Information is available from the Wiley Online Library or from the author.

Acknowledgements

X. J. and C.F. are grateful for the financial support from the U.S. National Science Foundation (NSF), Award No. CBET-2038381. X. J. and P. A. G. are thankful for the U.S. NSF Award No. DMR-2004636. K.G. thanks to the Japan Society for the Promotion of Science, KAKENHI Grant No. 20H00399 in partial support of the nuclear magnetic resonance measurements.

Received: ((will be filled in by the editorial staff))

Revised: ((will be filled in by the editorial staff))

Published online: ((will be filled in by the editorial staff))

References

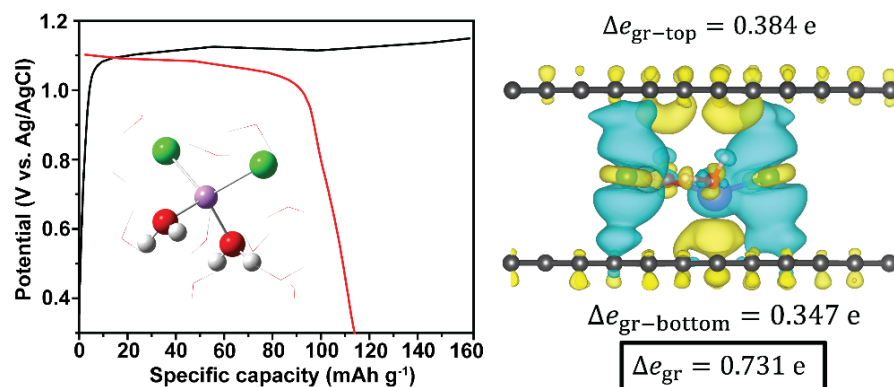
- [1] X. Zhou, Q. Liu, C. Jiang, B. Ji, X. Ji, Y. Tang, H. M. Cheng, *Angew. Chem. Int. Ed.* **2020**, *59*, 3802-3832.
- [2] T. Placke, A. Heckmann, R. Schmuck, P. Meister, K. Beltrop, M. Winter, *Joule* **2018**, *2*, 2528-2550.
- [3] I. A. Rodríguez-Pérez, X. Ji, *ACS Energy Lett.* **2017**, *2*, 1762-1770.
- [4] J. B. Goodenough, K.-S. Park, *J. Am. Chem. Soc.* **2013**, *135*, 1167-1176.

- 1 [5] Y. Sui, C. Liu, R. C. Masse, Z. G. Neale, M. Atif, M. AlSalhi, G. Cao, *Energy Storage*
- 2 *Materials* **2020**, 25, 1-32.
- 3 [6] L. Zhang, H. Wang, X. Zhang, Y. Tang, *Adv. Funct. Mater.* **2021**, 31, 2010958.
- 4 [7] W. Rüdorff, U. Hofmann, Z. Anorg. *Allg. Chem.* **1938**, 238, 1-50.
- 5 [8] F. P. McCullough, C. A. Levine, R. V. Snelgrove, Google Patents, 1989.
- 6 [9] R. Carlin, J. Fuller, W. Kuhn, M. Lysaght, P. Trulove, *J. Appl. Electrochem.* **1996**, 26,
- 7 1147-1160.
- 8 [10] R. T. Carlin, C. Hugh, J. Fuller, P. C. Trulove, *J. Electrochem. Soc.* **1994**, 141, L73.
- 9 [11] S. Rothermel, P. Meister, G. Schmuelling, O. Fromm, H.-W. Meyer, S. Nowak, M.
- 10 Winter, T. Placke, *Energy Environ. Sci.* **2014**, 7, 3412-3423.
- 11 [12] J. Holoubek, Y. Yin, M. Li, M. Yu, Y. S. Meng, P. Liu, Z. Chen, *Angew. Chem. Int.*
- 12 *Ed.* **2019**, 58, 18892-18897.
- 13 [13] J. Lang, J. Li, F. Zhang, X. Ding, J. A. Zapien, Y. Tang, *Batteries Supercaps* **2019**, 2,
- 14 440-447.
- 15 [14] Y. Kondo, Y. Miyahara, T. Fukutsuka, K. Miyazaki, T. Abe, *Electrochem. Commun.*
- 16 **2019**, 100, 26-29.
- 17 [15] X. Wu, Y. Xu, C. Zhang, D. P. Leonard, A. Markir, J. Lu, X. Ji, *J. Am. Chem. Soc.*
- 18 **2019**, 141, 6338-6344.
- 19 [16] C. Zhang, J. Holoubek, X. Wu, A. Daniyar, L. Zhu, C. Chen, D. P. Leonard, I. A.
- 20 Rodríguez-Pérez, J.-X. Jiang, C. Fang, *Chem. Commun.* **2018**, 54, 14097-14099.
- 21 [17] I. A. Rodríguez-Pérez, L. Zhang, D. P. Leonard, X. Ji, *Electrochem. Commun.* **2019**,
- 22 109, 106599.
- 23 [18] Q. Guo, K. i. Kim, H. Jiang, L. Zhang, C. Zhang, D. Yu, Q. Ni, X. Chang, T. Chen, H.
- 24 Xia, *Adv. Funct. Mater.* **2020**, 30, 2002825.
- 25 [19] Q. Guo, K.-I. Kim, S. Li, A. M. Scida, P. Yu, S. K. Sandstrom, L. Zhang, S. Sun, H.
- 26 Jiang, Q. Ni, *ACS Energy Lett.* **2021**, 6, 459-467.
- 27 [20] K. i. Kim, Q. Guo, L. Tang, L. Zhu, C. Pan, C. h. Chang, J. Razink, M. M. Lerner, C.
- 28 Fang, X. Ji, *Angew. Chem. Int. Ed.* **2020**, 59, 19924-19928.
- 29 [21] M.-C. Lin, M. Gong, B. Lu, Y. Wu, D.-Y. Wang, M. Guan, M. Angell, C. Chen, J.
- 30 Yang, B.-J. Hwang, *Nature* **2015**, 520, 324-328.
- 31 [22] M. Angell, C.-J. Pan, Y. Rong, C. Yuan, M.-C. Lin, B.-J. Hwang, H. Dai, *Proc. Natl.*
- 32 *Acad. Sci. U. S. A.* **2017**, 114, 834-839.
- 33 [23] D.-Y. Wang, C.-Y. Wei, M.-C. Lin, C.-J. Pan, H.-L. Chou, H.-A. Chen, M. Gong, Y.
- 34 Wu, C. Yuan, M. Angell, *Nat. Commun.* **2017**, 8, 1-7.

- 1 [24] P. Bhauriyal, A. Mahata, B. Pathak, *Phys. Chem. Chem. Phys.* **2017**, 19, 7980-7989.
- 2 [25] K. V. Kravchyk, S. Wang, L. Piveteau, M. V. Kovalenko, *Chem. Mater.* **2017**, 29,
- 3 4484-4492.
- 4 [26] X.-B. Wang, C.-F. Ding, L.-S. Wang, A. I. Boldyrev, J. Simons, *J. Chem. Phys.* **1999**,
- 5 110, 4763-4771.
- 6 [27] S. Agarwal, A. M. Hossain, Y.-S. Choi, M. Cheong, H. G. Jang, J. S. Lee, *Bull.*
- 7 *Korean Chem. Soc.* **2013**, 34, 3771-3776.
- 8 [28] L. Zhu, W. Liu, C. Fang, *Appl. Phys. Lett.* **2014**, 105, 041106.
- 9 [29] I. Juurinen, T. Pylkkanen, K. O. Ruotsalainen, C. J. Sahle, G. Monaco, K.
- 10 Hamalainen, S. Huotari, M. Hakala, *J. Phys. Chem. B.* **2013**, 117, 16506-16511.
- 11 [30] A. P. Gaiduk, G. Galli, *J. Phys. Chem. Lett.* **2017**, 8, 1496-1502.
- 12 [31] L. Petit, R. Vuilleumier, P. Maldivi, C. Adamo, *J. Chem. Theory Comput.* **2008**, 4,
- 13 1040-1048.
- 14 [32] Y. Zeng, C. Wang, X. Zhang, S. Ju, *Chem. Phys.* **2014**, 433, 89-97.
- 15 [33] Pethes, *J. Mol. Liq.* **2018**, 264, 179-197.
- 16 [34] T. Seki, K.-Y. Chiang, C.-C. Yu, X. Yu, M. Okuno, J. Hunger, Y. Nagata, M. Bonn, *J.*
- 17 *Phys. Chem. Lett.* **2020**, 11, 8459-8469.
- 18 [35] Pavlović, M.; Baranović, G.; Lovreković, D., *Spectrochim. Acta A* **1991**, 47, 897-906.
- 19 [36] B. M. Meyer, N. Leifer, S. Sakamoto, S. G. Greenbaum, C. P. Grey, *Electrochem.*
- 20 *Solid-State Lett.* **2005**, 8, A145.
- 21 [37] K. Zaghib, K. Tatsumi, Y. Sawada, S. Higuchi, H. Abe, T. Ohsaki, *J. Electrochem.*
- 22 *Soc.* **1999**, 146, 2784.
- 23 [38] J.-S. Zheng, L. Zhang, A. Shellikeri, W. Cao, Q. Wu, J. P. Zheng, *Sci. Rep.* **2017**, 7, 1-
- 24 8.
- 25 [39] B. Soberats, M. Yoshio, T. Ichikawa, H. Ohno, T. Kato, *J. Mater. Chem. A* **2015**, 3,
- 26 11232-11238.
- 27 [40] Z.-L. Xu, G. Yoon, K.-Y. Park, H. Park, O. Tamwattana, S. J. Kim, W. M. Seong, K.
- 28 Kang, *Nat. Commun.* **2019**, 10, 1-10.
- 29 [41] C. Fang, L. Tang, B. G. Oscar, C. Chen, *J. Phys. Chem. Lett.* **2018**, 9, 3253-3263.
- 30 [42] L. Tang, L. Zhu, M. A. Taylor, Y. Wang, S. J. Remington, C. Fang, *Molecules* **2018**, 23,
- 31 2226.
- 32 [43] C. Zhang, W. Shin, L. Zhu, C. Chen, J. C. Neuefeind, Y. Xu, S. I. Allec, C. Liu, Z. Wei,
- 33 A. Daniyar, *Carbon Energy* **2021**, 3, 339-348.

- [44] M. Frisch, G. Trucks, H. Schlegel, G. Scuseria, M. Robb, J. Cheeseman, G. Scalmani, V. Barone, G. Petersson, H. Nakatsuji, *Gaussian, Inc. Wallingford CT* **2016**.
- [45] L. Petit, R. Vuilleumier, P. Maldivi, C. Adamo, *J. Chem. Theory Comput.* **2008**, *4*, 1040-1048.
- [46] I. Pethes, *J. Mol. Liq.* **2018**, *264*, 179-197.
- [47] C. Chen, J. N. Tutol, L. Tang, L. Zhu, W. S. Ong, S. C. Dodani, C. Fang, *Chem. Sci.* **2021**, *12*, 11382-11393.
- [48] G. Kresse, J. Furthmüller, J. Hafner, *Phys. Rev. B* **1994**, *50*, 13181.
- [49] G. Kresse, J. Furthmüller, *Comput. Mater. Sci.* **1996**, *6*, 15-50.
- [50] G. Kresse, J. Furthmüller, *Phys. Rev. B* **1996**, *54*, 11169.
- [51] J. P. Perdew, K. Burke, M. Ernzerhof, *Phys. Rev. Lett.* **1996**, *77*, 3865.
- [52] K. Mathew, R. Sundararaman, K. Letchworth-Weaver, T. Arias, R. G. Hennig, *J. Chem. Phys.* **2014**, *140*, 084106.
- [53] W. Tang, E. Sanville, G. Henkelman, *J. Condens. Matter Phys.* **2009**, *21*, 084204.

Entry for the Table of Contents



Highly concentrated water-in-salt electrolytes (WiSE) or deep eutectic solvents (DES) electrolytes are promising alternatives to organic electrolytes in terms of the cost and the safety. Here, we present a DES electrolyte comprising 20 *m* LiCl + 20 *m* ChCl to demonstrate the reversible storage of the lightest superchloride, [LiCl₂]⁻, in graphite cathode of aqueous dual-ion battery. Storage of this superchloride in graphite exhibits a reversible capacity of 110 mAh g⁻¹ over 400 cycles, which renders graphite partially turbostratic upon cycling. Stimulated Raman analysis identified [Li(H₂O)₂Cl₂]⁻ as a dominant anionic species. NMR results and DFT calculations reveal the insertion of hydrated [LiCl₂]⁻ in between graphene layers is energetically favorable over dehydrated anions. This study opens up the potential for the further exploration on water-based graphite intercalation compounds (GICs).

Supporting Information

Reversible Insertion of $[\text{LiCl}_2]^-$ Superhalides in Graphite Cathode of Dual-Ion Batteries

Keun-il Kim, Longteng Tang, Pegah Mirabedini, Amika Yokoi, Jesse M. Muratli, Qiubo Guo, Prof. Michael M. Lerner, Prof. Kazuma Gotoh*, Prof. P. Alex Greaney*, Prof. Chong Fang* and Prof. Xiulei Ji*

Table S1. Performance of superhalides as anion charge carriers. Note that, $[\text{ZnCl}_4]^{2-}$, a divalent superchalcogenide, is included in this table as a parallel category to superhalides.

Charge carrier	Electrolyte	Compound	Avg. reversible capacity (mAh g ⁻¹)	Avg. CE (%)	Cycle life
$[\text{AlCl}_4]^-$	1.3 : 1 AlCl_3 + $[\text{EMIm}]\text{Cl}^{[1]}$	graphite	60	98.1	200
$[\text{AlCl}_4]^-$	1.3 : 1 AlCl_3 + Urea ^[2]	graphite	73	99.7	200
$[\text{AlCl}_4]^-$	1:1 AlCl_3 + $[\text{DMPI}]\text{Cl}^{[3]}$	graphite	80	97	300
$[\text{ZnCl}_4]^{2-}$	30 m ZnCl_2 ^[4]	$\text{Zn}_3[\text{Fe}(\text{CN})_6]_2$	48	100	1000
$[\text{ZnCl}_4]^{2-}$	30 m ZnCl_2 ^[5]	nitrogen-doped few-layered graphene	82	97	800
$[\text{MgCl}_3]^-$	9 m MgCl_2 + 30 m $\text{ChCl}^{[6]}$	graphite	78	98	300
$[\text{LiCl}_2]^-$	20 m LiCl + 20 m ChCl (This work)	graphite	108	97.8	450

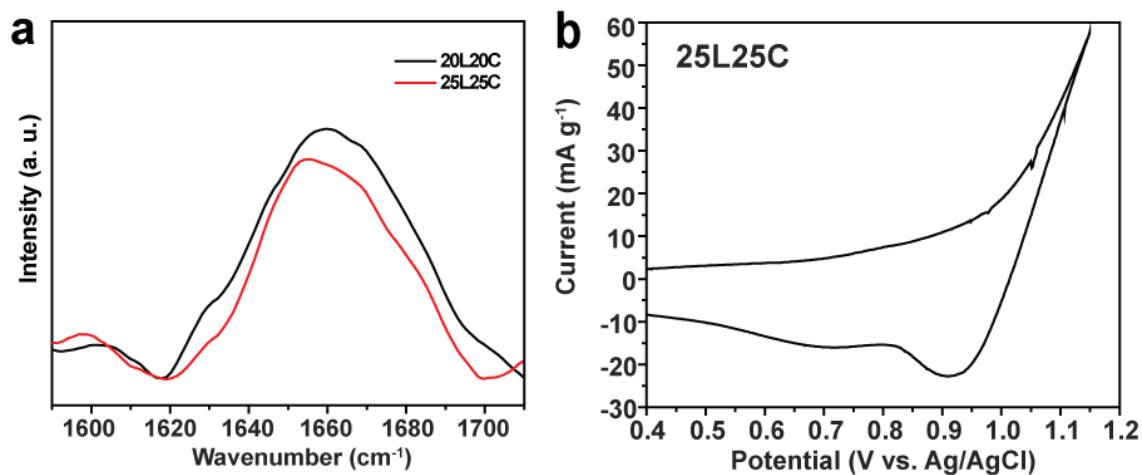


Figure S1. (a) Stimulated Raman spectra for the H–O–H bending mode for the mixed electrolytes 20L20C (black) and 25L25C (red). The main peak intensity decrease from 20L20C to 25L25C is notable, which represents a reverse of the increasing trend from 5L20C, 10L20C, to 20L20C (higher polarizability of water bending modes in contact with Li⁺ than with Ch⁺). (b) CV curve of graphite in 25L25C.

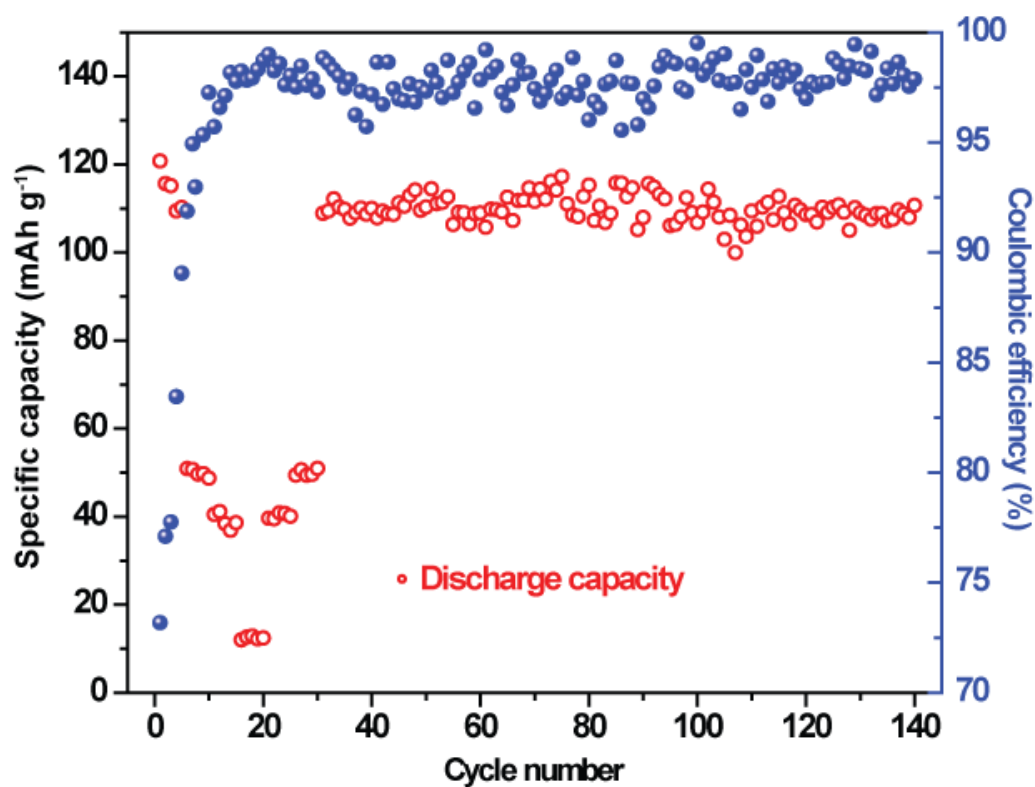


Figure S2. Rate performance of graphite electrode in 20L20C. Current rate applied is: 50 mA g⁻¹ (from the 1st to the 5th cycle); 100 mA g⁻¹ (from the 6th to the 10th cycle); 200 mA g⁻¹ (from the 11th to the 15th cycle); 400 mA g⁻¹ (from the 16th to the 20th cycle); 200 mA g⁻¹ (from the 21st cycle to the 25th cycle); 100 mA g⁻¹ (from the 26th cycle to the 30th cycle); and 50 mA g⁻¹ for the following cycles.

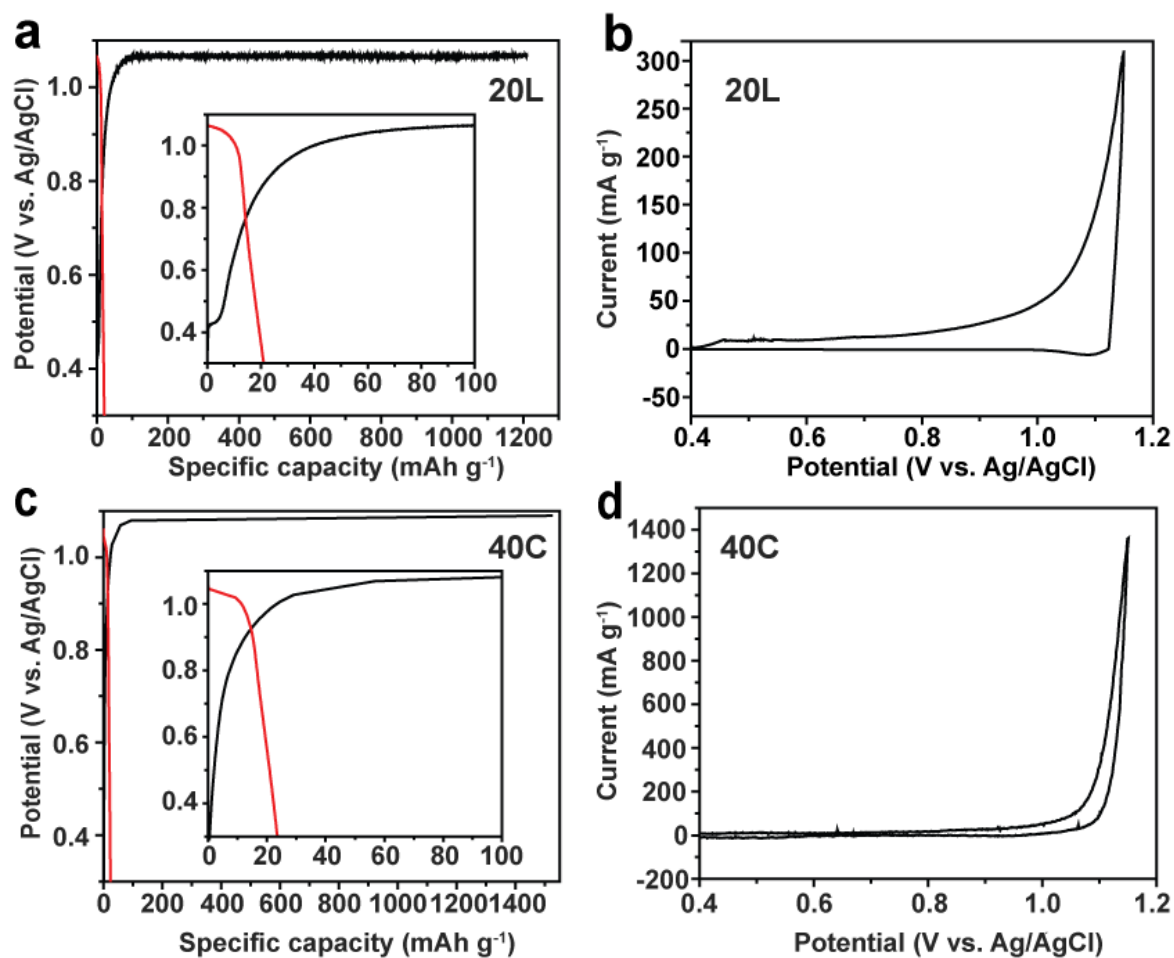


Figure S3. Electrochemical characterization of graphite in saturated single salt solutions. (a) 1st cycle GCD profiles; (b) CV curve in 20L; (c) 1st cycle GCD profiles; (d) CV curve in 40C. 50 mA g⁻¹ of current rate and 0.1 mV s⁻¹ scan rate were applied.

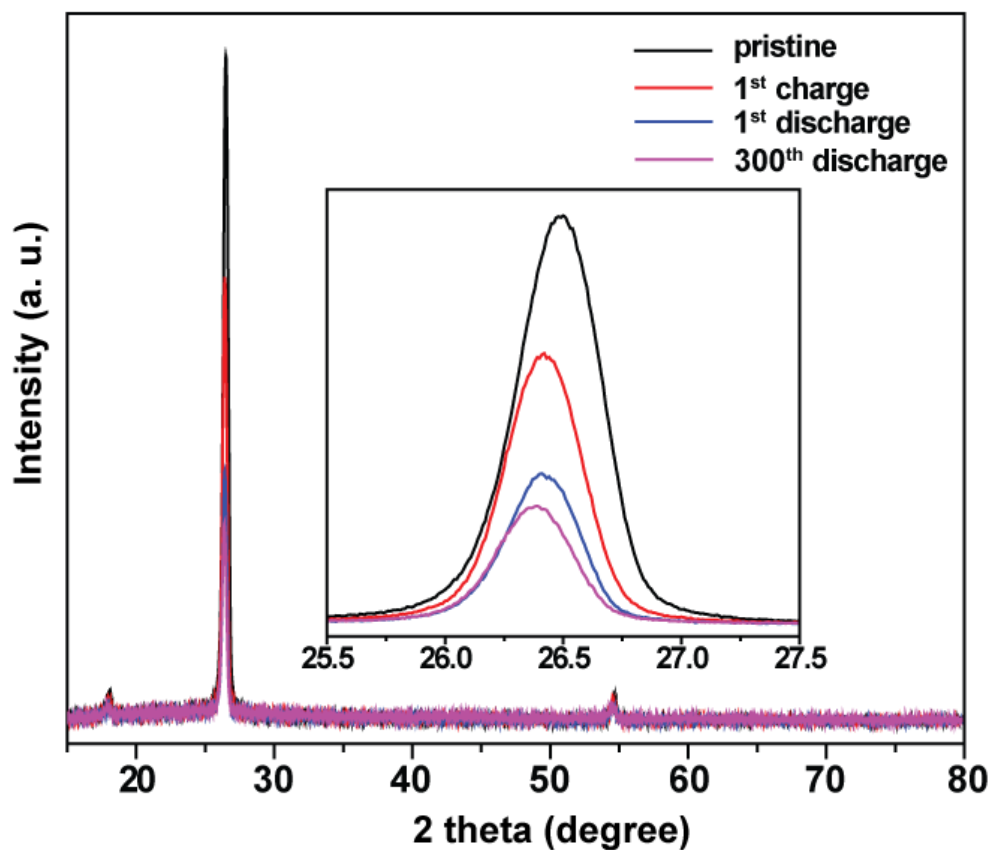


Figure S4. XRD patterns of graphite electrodes at different state of charge (SOC) of the first cycle and after the 300th cycle: pristine (black), after the first charge (red), and after the first discharge (blue), and at the end of the 300th cycle (purple). The inset represents a peak for the (002) planes of graphite.

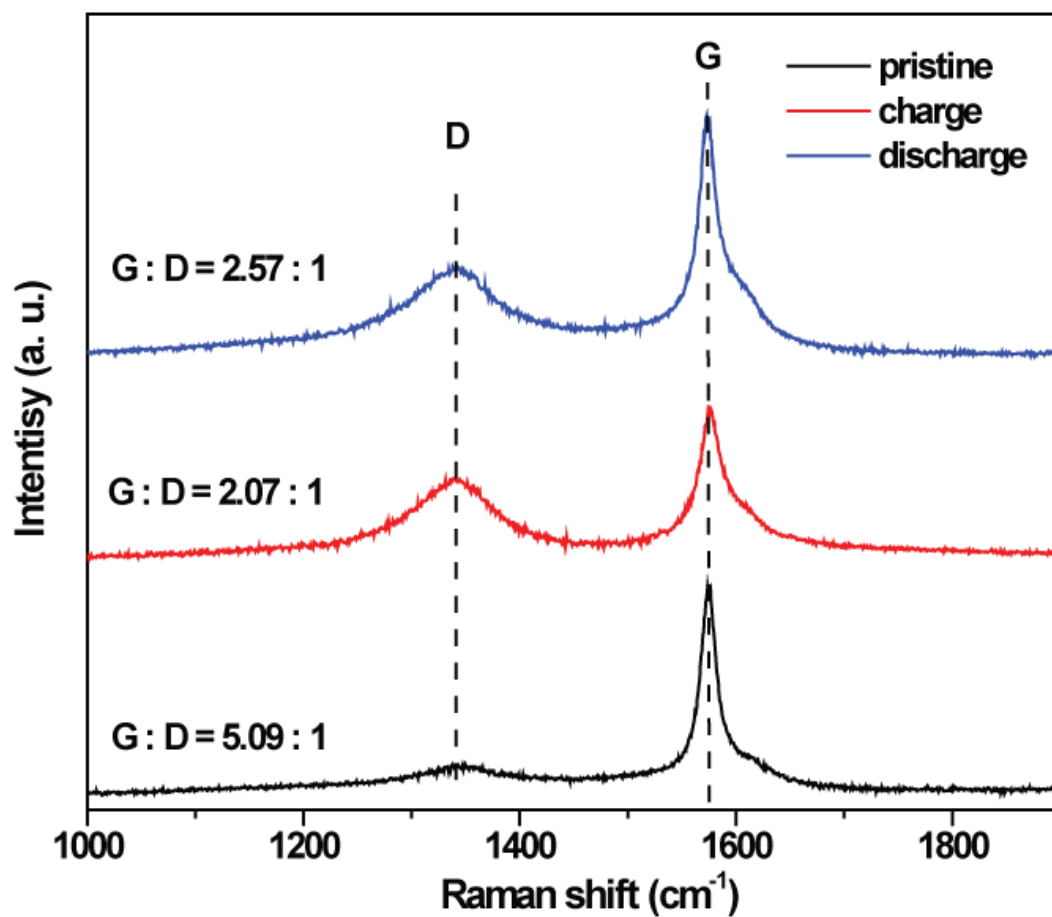


Figure S5. Spontaneous Raman spectra of graphite electrodes at different SOC: pristine (black), charge (red), and discharge (blue). The G and D marker bands are denoted by vertical dashed lines with their intensity ratios listed in the inset.

Table S2. Analysis of elemental concentration and ratio of graphite in 20L20C by ICP-MS at different SOC in the 1st cycle at a current rate of 50 mAh g⁻¹, with concentrated nitric acid as a leaching agent. “Charge” denotes graphite charged to 1.15 V (with anions being inserted); and “Discharge” denotes graphite discharged to 0.3 V (with anions being de-inserted).

	Mass concentration		Molar concentration		Ratio
Sample	Cl ⁻ (μg/ml)	Li ⁺ (μg/ml)	Cl ⁻ (μmol/L)	Li ⁺ (μmol/L)	Cl ⁻ /Li ⁺ (mol/mol)
Charge	661 (± 8)	57.0 (± 3.0)	18644 (± 226)	8212 (± 432)	2.3 (± 0.1)
Discharge	109 (± 8)	4.79 (± 0.03)	3074 (± 226)	691 (± 4)	4.5 (± 0.3)

DFT Calculation of potential intercalation compounds at full storage capacity

The DFT calculations in the main text established that for insertion of a lone ion, it is easier for the LiCl_2^- anions to be inserted into bilayer graphene if it is hydrated rather than dehydrated. To study if the inserted anions interact, we have also performed calculations for pairs of ions inserted into bilayer graphene with a density equivalent to the full storage capacity of 114 mAh g^{-1} . In these calculations the structure was initiated with the ions in the same geometry as in configuration B, which had the lowest insertion energy. The calculations were set up with the ions initially away from high symmetry positions so that the ions were able to attract or repel without geometric constraint. During structural relaxation the ions arrange into a stripped packing in which the ions have alternating orientation so that the water molecules from one ion coordinate to the chloride in its neighbor as shown in **Figure S6a**. In this interacting structure the hydrated ions flatten, becoming completely planar. The energy for ion insertion in this structure is 0.50 eV per ion lower (easier) than for the non-interacting ions at $2/3$ full capacity. In this configuration the graphene interlayer spacing is slightly widened from 6.2 to 6.4 \AA . Bader charge analysis of this intercalation compound shows that when the anions are inserted there is a charge transfer of 0.35 electrons per ion to the graphene. This calculation is not the product of an exhaustive search for the lowest energy packing of the ions, and so it is likely that the structure is not the global minimum energy packing. However, this packing yields an anion insertion energy that is significantly lower than that of the lone ions. Our results suggest that during insertion, the ions agglomerate into a structure similar to this configuration and fill the graphene in a cooperative way.

These calculations also reveal the role that co-inserted water plays. The water is not a spectator that is carried along for the ride but acts as water of crystallization in this 2D packing enabling closer packing of the ions. To elucidate this, we have relaxed this structure with the water molecules removed. In this case, the LiCl_2^- anions pair up to form lozenge-shaped packing of Li_2Cl_4 . These ions are then surrounded by chloride ions, so it is not possible to arrange them to form a continuous intercalation compound. The insertion energy for these paired non-hydrated anions at full capacity is 1.1 eV larger (less favorable) than for the hydrated ions at the same capacity. The packing of non-hydrated ions expands the graphite galleries by the same amount as the hydrated ions, and so there is also no size compatibility advantage for insertion of non-hydrated ions.

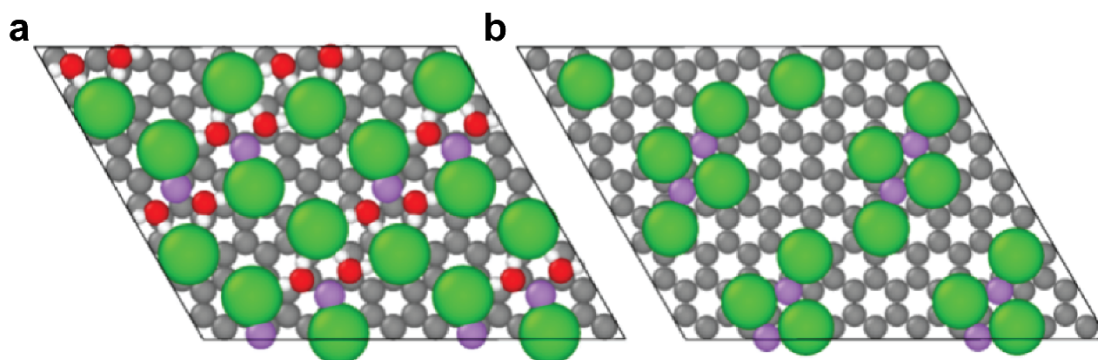


Figure S6. (a) Relaxed structure of one possible configuration for the hydrated $[\text{Li}(\text{H}_2\text{O})_2\text{Cl}_2]^-$ ions in the graphite intercalation compound at 114 mAh g^{-1} capacity. The grey, green, purple, red and white atoms correspond to C, Cl, Li, O and H, respectively. The top graphene sheet has been removed for clarity. The ions and water molecules are completely planar. (b) The structure that is obtained after removing the water molecules from the structure in (a) and letting the atoms relax.

References

- [1] M.-C. Lin, M. Gong, B. Lu, Y. Wu, D.-Y. Wang, M. Guan, M. Angell, C. Chen, J. Yang, B.-J. Hwang, *Nature* **2015**, 520, 324-328.
- [2] M. Angell, C.-J. Pan, Y. Rong, C. Yuan, M.-C. Lin, B.-J. Hwang, H. Dai, *Proc. Natl. Acad. Sci. U. S. A.* **2017**, 114, 834-839.
- [3] Z. Lv, M. Han, J. Sun, L. Hou, H. Chen, Y. Li, M.-C. Lin, *J. Power Sources* **2019**, 418, 233-240.
- [4] X. Wu, Y. Xu, C. Zhang, D. P. Leonard, A. Markir, J. Lu, X. Ji, *J. Am. Chem. Soc.* **2019**, 141, 6338-6344.
- [5] Q. Guo, K. i. Kim, H. Jiang, L. Zhang, C. Zhang, D. Yu, Q. Ni, X. Chang, T. Chen, H. Xia, *Adv. Funct. Mater.* **2020**, 30, 2002825.
- [6] K. i. Kim, Q. Guo, L. Tang, L. Zhu, C. Pan, C. h. Chang, J. Razink, M. M. Lerner, C. Fang, X. Ji, *Angew. Chem. Int. Ed.* **2020**, 59, 19924-19928.